An Observational Study of the Role of Penetrating Cumulus in a Marine Stratocumulus-Topped Boundary Layer

QING WANG AND D. H. LENSCHOW

National Center for Atmospheric Research, Boulder, Colorado*

(Manuscript received 30 June 1994, in final form 3 January 1995)

ABSTRACT

Isolated cumuli penetrating through marine stratocumulus clouds were documented during the Atlantic Stratocumulus Transition Experiment. This paper aims at understanding the role of the penetrating cumulus in regulating stratocumulus and boundary-layer structure through analysis of data from the NCAR Electra aircraft. When penetrating cumulus clouds are present, the boundary layer is generally decoupled from the near-surface air except in the cumulus region. Therefore, air in the cumulus region includes air entrained at the cloud top, as well as air modified by surface processes. In the stratocumulus region, however, entrained inversion air and moist surface air are confined to separate layers. As a result, large horizontal variations are found in scalars, such as ozone and water vapor. Turbulence statistics and conditional sampling of entrainment events in the cumulus and stratocumulus regions indicate that stronger entrainment may occur at the cumulus top compared to the surrounding stratocumulus. This analysis is, however, complicated by insufficient sampling of cloud-top jump conditions in both regions.

Convergent flow in the lower boundary layer and compensating diverging flow in the upper boundary layer were identified along the flight track. This flow field, together with the vertical coupling of surface air with the cloud layer in the cumulus region, helps to transport moisture upwards from the sea surface and disperse it to the surrounding stratocumulus sheet, thus helping to maintain the stratocumulus cover.

1. Introduction

There are two distinct cloud regimes along a trade wind trajectory that passes over a progressively warmer sea surface. At the upwind end of this trajectory, extensive sheets of low-level stratocumulus are observed over the relatively cool water off the west coast of major continents (e.g., along the eastern Pacific). Downstream near the equator, fields of trade cumulus cloud are found in a deeper atmospheric boundary layer. While both regimes are important in the global radiation budget, their effects on climate are different because of substantial differences in cloud and boundary-layer turbulence structures in the two cloud regimes. Subtropical stratocumulus-topped boundary layers are generally shallower, nearly fully covered by clouds, and topped by a strong capping inversion (Hanson 1991). Trade cumulus boundary layers, in contrast, are in a weaker subsiding region with a weaker capping inversion. A typical range of cloud coverage for trade cumulus cloud is 20%–30% (Warren et al. 1989).

While the structures of the two types of boundary layer at either end of the low-level trade wind trajectory have been studied extensively (e.g., Nicholls 1984; Hignett 1991; Q. Wang 1993; Pennell and LeMone 1974; LeMone and Pennell 1976; Albrecht et al. 1979; and Bretherton 1993), the transition from one to the other is poorly understood. This topic has not been extensively studied, although S. Wang (1993) and Krueger et al. (1994) have carried out model simulations, and Paluch et al. (1994) have analyzed and compared observations from separate experiments in each region. Yet, this transition is important in understanding the factors that regulate cloud type and amount in the boundary layer and, therefore, in providing proper parameterization of boundary-layer clouds and turbulence in climate models. The Atlantic Stratocumulus Transition Experiment (ASTEX) was designed to study this transition and cloud-mode selection. This experiment was conducted in June 1992 in the area of the Azores and the Madeira Islands, where a transition from a stratocumulus to a trade wind cumulus regime often occurs. A daily summary of the field operations, synoptic situations, soundings, and satellite imagery is reported by Bluth and Albrecht (1993a,b).

During ASTEX, cumulus clouds were observed to occur frequently under stratocumulus sheets and to persist for hours with little evolution (Kropfli and Orr 1993). They may be energetic enough to penetrate into

* The National Center for Atmospheric Research is sponsored by the National Science Foundation.

Corresponding author address: Dr. Qing Wang, NCAR/MMM, P.O. Box 3000, Boulder, CO 80307-3000.

the overlying stratocumulus. A photograph of this cloud structure, taken on 17 June 1992 during ASTEX, is shown in Fig. 1. Besides the many small cumuli below the stratocumulus cover, well-developed cumuli that penetrate through the stratocumulus top were also observed, resulting in a higher cloud top compared to the surrounding stratocumulus. In some cases, the stratocumulus clouds dissipated elsewhere except on top of the penetrating cumuli. Radar observations (Kropfli and Orr 1993) show that the reflectivity cores in the penetrating cumuli are generally 1–2 km in diameter, with a much larger enhanced patch of stratocumulus approximately 15–20 km across. Visual estimates (ASTEX observer's notes) of the diameter of the cumuli are generally several kilometers.

Small cumuli under solid or broken stratocumulus clouds have been observed previously [e.g., near the California coast during the First ISCCP Regional Experiment (FIRE), Q. Wang 1993]. They are, however, distinctly different from the penetrating cumuli observed during ASTEX and discussed here. In addition to their larger size and stronger dynamic intensity, the latter are isolated events and penetrate through the overlying stratocumulus. Bretherton (1992) proposed in his conceptual model of cloud transition that this cloud type is an important stage in the transition process. Paluch and Lenschow (1991) also suggested in a conceptual model that cumulus clouds may form and develop below the stratocumulus layer and interact with the stratocumulus. Quantitatively, however, little is known about the roles the penetrating cumuli play.

In this study, we use measurements from the National Center for Atmospheric Research's (NCAR) Electra aircraft to study the role of these penetrating cumuli in regulating stratocumulus and boundary-layer structure. The measurements are from Flight 4 on 10 June 1992 during ASTEX, when the aircraft flew in and below penetrating cumulus and stratocumulus at several levels in the boundary layer. Two issues are of particular interest to us: 1) What role do penetrating cumuli play in transporting moisture and other scalars between the sea surface and the top of the boundary layer? 2) Do the overshooting cumuli significantly impact the cloud-top entrainment process? These two issues are directly related to the important question of whether the penetrating cumuli tend to break up or maintain the overlying stratocumulus clouds.

In the following sections, we first give a brief description of the flight and meteorological conditions. Evidence of penetrating cumuli and observations of the horizontal wind field around the cumuli at several levels are then presented. We next focus on analyzing the effects of cumuli in coupling the stratocumulus layer with the underlying boundary layer and in the entrainment process near cloud top. The importance of cumulus in the evolution of stratocumulus cloud will be discussed in the last section.

FIG. 1. Photograph of the boundary-layer clouds, showing a penetrating cumulus in the center of the picture and many small cumuli under the stratocumulus deck. The picture was taken on 17 June 1992 in the same general area as the case analyzed in this study (Courtesy of C. Bretherton, University of Washington).

2. Instrumentation and meteorological conditions

The major variables used in this study are temperature, water vapor mixing ratio, ozone concentration, vertical and horizontal winds, and liquid water. These are available at a sampling rate of 20 s^{-1}. Temperature was measured with a Rosemount resistance wire thermometer. We compared the output of this sensor with an OPHIR radiometric temperature sensor and found that wetting by cloud water is not a problem here. Liquid water was measured with a Particle Measurements Systems Forward Scattering Spectrometer Probe (FSSP). There are uncertainties about the absolute calibration of liquid water measured with the FSSP, but this does not significantly affect our results since we are concerned mainly with differences in liquid water. Absolute humidity was measured with a Lyman-alpha hygrometer, using a dewpoint hygrometer as an absolute reference. The measurement is reliable for humidity fluctuations below cloud but is affected by liquid water in cloud. As a result, we use the mixing ratio measured by the CSIRO total water sensor for the in-cloud legs, although it is available at a rate of only 1 s^{-1}. The nitric oxide chemiluminescence ozone sensor used during ASTEX was developed by NCAR. There is some question about whether the measurement may be affected by liquid water (Richard Schillawski 1994, personal communication), but we were unable to see any obvious effects on ozone flux and variance from the in-cloud measurements.

Figure 2 shows an aircraft sounding taken before the first set of horizontal flight legs on Flight 4. On this day, the boundary layer in the research area was capped by nearly solid stratocumulus. The liquid water profile shows cloud top at about 1600 m and cloud base at about 1100 m. According to the observer's notes, the small spikes of liquid water around 1000 m are due to

wisps of cumuli below the stratocumulus. Boundary-layer decoupling is clearly seen in the profiles of water vapor and ozone mixing ratio. An abrupt decrease in water vapor mixing ratio (from the dewpoint hygrometer) and an increase in ozone mixing ratio with height at about 600 m denote the location of the decoupling transition layer. Below this level, the boundary layer is well mixed. Moderate wind of about 6 m s^{-1} was observed throughout the entire boundary layer. Some wind shear is observed in the decoupling transition layer, which is more obvious in the sounding taken two hours later (not shown here).

The boundary layer is capped by a temperature inversion of 4.5 K. Across the inversion base, water vapor decreases by about 5 g kg^{-1}, and ozone increases by about 9 ppbv. Using the criterion in Randall (1980), the cloud-top jump conditions suggest instability owing to cloud-top entrainment.

To evaluate the potential for cumulus development, we estimated the convective available potential energy (CAPE) to be 12 J kg^{-1} from the sounding shown in Fig. 2. This corresponds to a maximum possible vertical velocity of 4.9 m s^{-1}. The lifting condensation level calculated from this sounding is at 925 mb. Although the CAPE here is nearly two orders of magnitude smaller than that characteristic of a deep convective system, it is sufficient to provide energy for air parcels to penetrate through the decoupling transition layer (Q. Wang 1993).

Five levels in the boundary layer were sampled within two hours. The height, length, and time period of each horizontal traverse are tabulated in Table 1. The flight legs were nearly perpendicular to the boundary-layer mean wind and were flown so that the aircraft flight tracks advected with the wind; that is, if the mean wind trajectory had been subtracted from the horizontal projection of the flight track (Fig. 3), then the flight legs would be nearly on top of each other. Thus, the measurements are nominally within the same air mass. Since the cumulus clouds usually have a diameter of several kilometers, it is almost certain that the aircraft was sampling the same cloud structures on successive legs.

TABLE 1. Description of the horizontal flight legs analyzed in this study.

Leg	Start time (LST)	End time (LST)	Height (m)	Length (km)
1	0630:48	0645:34	30	88.6
2	0649:00	0704:00	610	90.0
3	0707:00	0721:30	914	87.0
4	0724:20	0739:15	1281	89.5
5	0741:50	0757:00	1524	91.0

3. The penetrating cumuli

As illustrated in Fig. 1, several penetrating cumulus clouds with bases below the stratocumulus layer were reported by the onboard observer on 10 June 1992. Figure 4 shows that the horizontal flight legs passed through such cumulus clouds. Figures 4a and 4b show the liquid water content sampled at the 1524-m (leg 5) and 1281-m (leg 4) levels, respectively. Both were within the solid stratocumulus layer. We note two liquid water peaks in the middle of both legs, which are so close that they are likely parts of the same cloud structure. The peak liquid water content reaches as high as 0.4 g m^{-3}, compared with 0.2 g m^{-3} for the rest of the legs. This difference in liquid water content strongly suggests enhancement by a process different from that occurring in the surrounding stratocumulus. This conclusion is supported by measurement of cloud

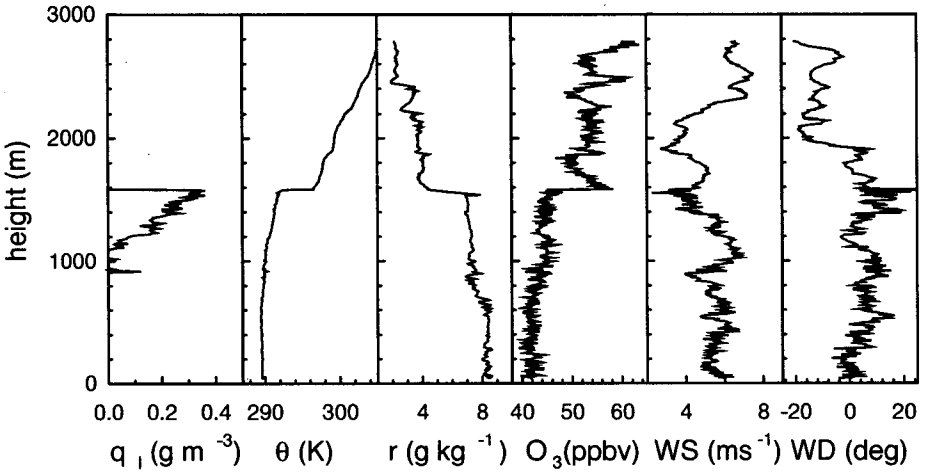

FIG. 2. Profiles of liquid water, potential temperature, mixing ratio, ozone concentration, wind speed, and wind direction from a descent between 0620:08 and 0627:49 (LST) on 10 June 1992.

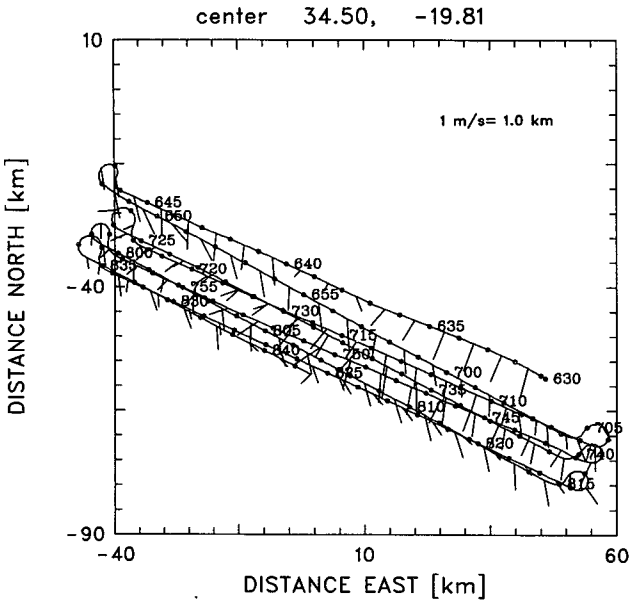

FIG. 3. Horizontal projection of the Electra flight track from the first vertical stack on 10 June 1992. The numbers beside the track are time in LST. The small bars denote the wind speed and direction. The graph is centered at 34.00°N latitude and 19.80°W longitude. The vertical axis shows distance from the center in the north–south direction; the horizontal axis is the same except in the east–west direction.

base height by an upward-looking infrared lidar from the flight leg at 30 m above the sea surface. Figure 4c shows the location of a strong reflecting boundary at the cloud base. The points above the primary reflecting boundary at the cloud base are likely artifacts and not related to the cloud structure. Here, lidar data below about 1000 m are within the lidar dead zone and are to be ignored. Figure 4c shows that there are two primary regions at 0637:30 and 0639:10 where the cloud base is much lower than that of the surroundings. The low cloud base regions correspond well with the liquid water peaks in the upper boundary layer. In addition, the aircraft observer recorded a higher cloud top around the center of the highest turbulence leg (leg 5). Therefore, we conclude that the aircraft went through two penetrating cumulus towers, similar to the one shown in the center of Fig. 1, over the middle section of the turbulence legs. Since these two cumulus clouds are very close to each other, and likely part of the same cloud structure, we will consider the middle region as the penetrating cumulus region. As a first approximation, we chose measurements from 0729:30 to 0735:00 (LST) on leg 4 and from 0747:00 to 0753:00 (LST) on leg 5 to represent the penetrating cumulus region at the two levels. Since the intervening region between the two peaks is small (about 1 min, or 6 km) compared with the combined Cu region (about 36 km), this approximation should not significantly affect the results.

The method used above to differentiate cumulus cloud from the surrounding stratocumulus is fairly qualitative. In an attempt to quantify this differentiation, we compared microphysical structure (e.g., the drop-size spectrum) in the assumed cumulus region with that in the surrounding stratocumulus. This method was not, however, successful, as there are too many factors that determine the microphysics of both cumulus and stratocumulus clouds.

To compare the mean and turbulent characteristics of the stratocumulus with the penetrating cumulus regions, we also select a section of data in the stratocumulus region at each in-cloud level. The stratocumulus region is selected such that the data at each leg represent nearly the same patch of stratocumulus at different levels. The measurements between 0724:30 and 0729:30 (LST) and between 0753:00 and 0757:00 (LST) are selected as the stratocumulus regions on legs 4 and 5, respectively. For brevity, we call the cumulus region the Cu region and the stratocumulus region the Sc region. These selections are all based on the liquid water content shown in Fig. 4.

4. Flow fields around the penetrating cumulus region

Figure 5 shows the alongtrack wind component (u_x) at five levels in the boundary layer. The left side of the graph always corresponds to the northwest end of the flight track (Fig. 2), while the right side corresponds to the southeast end. Our convention here is to define u_x as positive for the wind blowing from the southeast end to the northwest end of the flight track. The top three panels in this figure show very similar horizontal wind distributions along the flight legs, where diver-

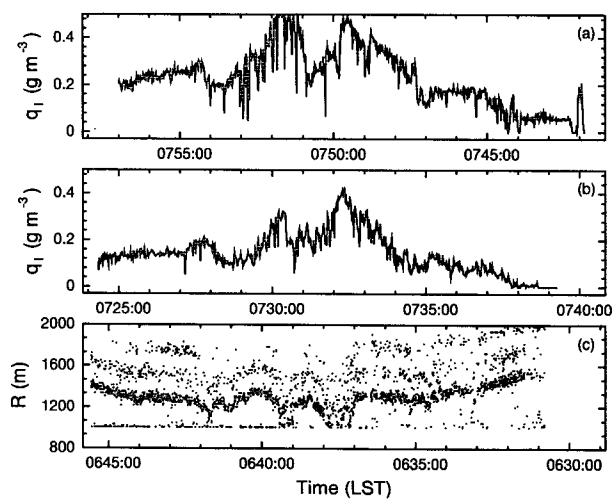

FIG. 4. (a) Liquid water content measured by the FSSP on leg 5. (b) Same as (a) except on leg 4. (c) Height of the cloud base obtained from an infrared lidar onboard the NCAR Electra at 30 m above the sea surface.

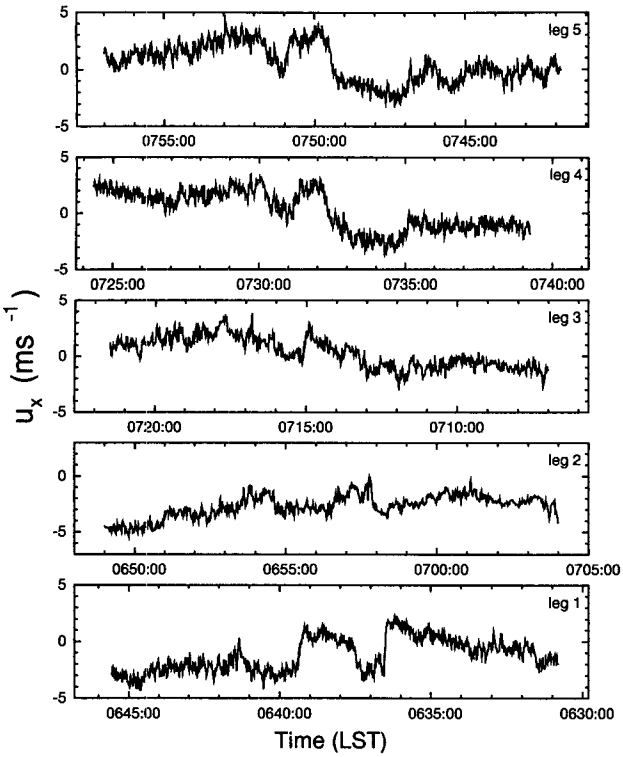

FIG. 5. Time series of the alongtrack wind component at five levels in the boundary layer described in Table 1.

gent flow is evident in the center of the leg. The area of distinct divergent flow corresponds well with the area occupied by the penetrating cumulus identified earlier. A crude estimate of the divergence along the flight track (i.e., neglecting cross-track contributions to the divergence) on leg 4 gives 2.9×10^{-4} s^{-1}, averaged over the region where an obvious slope of u_x is observed. Smaller divergence of 1.8×10^{-4} s^{-1} and 1.5×10^{-4} s^{-1} are found on legs 5 and 3, respectively. On leg 2, no obvious divergence or convergence flow pattern was observed in the middle region, although there appears to be convergent flow over the entire flight leg. On the lowest leg, the wind changes abruptly just below the cumulus base, resulting in local converging flow below the penetrating cumulus region. The convergence from the alongtrack wind component is estimated to be about -2.2×10^{-4} s^{-1} along this flight leg.

To check on the consistency of the above flow fields, we estimate the difference in mean vertical velocity between the Cu and Sc regions. First, we select sections of data that are measurements from the two regions. Since there is no direct indicator of cumulus cloud on the below-cloud legs (except on leg 1 as can be seen in Fig. 4c), this selection is based on characteristics of the flow field. We overlap the center of the convergent or divergent region in Fig. 5 and find the time periods on each below-cloud leg when the aircraft is just below the Cu and Sc region on the in-cloud legs. The selected Cu and Sc regions are tabulated in Table 2. The differences in mean vertical velocity between the Cu and Sc regions are given, since the mean itself is too small to measure directly (Lenschow and Spyers-Duran 1989). The accuracy of the velocity difference measurements is about 0.1 m s^{-1} (Lenschow and Spyers-Duran 1989). Therefore, the only significant velocity differences are found on legs 4 and 5. However, the vertical velocity measured on leg 5 (not shown) is dominated by a mesoscale variation at a timescale of around 5 min. The velocity difference calculated for this leg may be affected by this variation since it is obtained over an averaging length of around 30 km. Therefore, the result from leg 4, which shows relative mean upward motion in the cumulus region, may be the only significant measurement. In addition to the arbitrariness in selecting the Cu and Sc regions, we note that the aircraft may not have penetrated through the core of the cumulus, which may be only 1–2 km across. Using measurements from a ground-based Doppler radar, Kropfli and Orr (1993) found a narrow updraft of less than 1 km wide in the high-reflectivity core of a similar penetrating cumulus. They found that the vertical velocity inside the core can be 2 m s^{-1}.

5. Coupling of the boundary layer by penetrating cumulus

The sounding profiles (Fig. 2) indicate decoupling of the boundary layer at around 600 m. Decoupling is also evident in Fig. 6, where the cloud-base radiation temperature is compared with the temperature at the lifting condensation level (LCL), estimated from the 30-m flight leg (leg 1) data. The cloud-base temperature was obtained from an upward-facing PRT-5 radiation thermometer with an accuracy of about 1°C, and the LCL temperature was calculated from the in situ air temperature and water vapor mixing ratio. A temperature difference of more than 1°C suggests a decoupled boundary layer. This method of diagnosing decoupling in the stratocumulus-topped boundary layer is similar to that used by Q. Wang (1993) and Betts (1990), although they used cloud-base height from lidar observations.

TABLE 2. Time periods selected as the Cu and Sc regions on five horizontal flight legs, and the differences in mean updraft velocity between the two regions. Time is in LST.

Leg	Cu region (hhmmss)	Sc region (hhmmss)	$\bar{w}_{Cu} - \bar{w}_{Sc}$ (m s^{-1})
1	0635:30–0641:00	0641:00–0645:30	−0.002
2	0653:00–0700:00	0649:00–0653:00	−0.042
3	0711:00–0717:00	0717:00–0721:00	0.063
4	0729:30–0735:00	0724:30–0729:30	0.108
5	0747:00–0753:00	0753:00–0757:00	−0.119

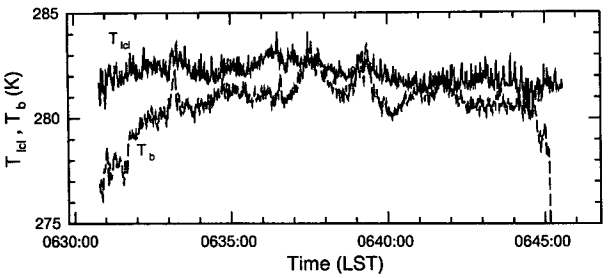

FIG. 6. Comparison of cloud-base temperature (T_b) measured by an upward-looking PRT-5 radiometer with temperature at the LCL. The LCL temperature is calculated from air temperature and moisture measured at 30 m above the sea surface (leg 1).

Figure 6 shows that the boundary layer is decoupled along most of the flight leg. However, close agreement between the two variables is seen in several regions (around 0637:30, 0639:10, and from 0640:30 to 0642:00 LST), suggesting that the boundary layer is well mixed in these areas. We pointed out earlier (Fig. 4) that the Electra passed just beneath the penetrating cumulus base around 0637:30 and 0639:00 (LST), which strongly suggests that the boundary layer is well mixed here because of the presence of cumulus. The other region of well-mixed boundary layer (between 0640:30 and 0642:00 LST) may well be related to cumulus clouds that were not vigorous enough to penetrate into the overlying stratocumulus.

6. Entrainment through stratocumulus and cumulus tops

To study entrainment at the immediate cloud top, we analyze data sampled during the two in-cloud legs only. Two types of analyses are done for the Cu and Sc regions. One is turbulent statistics; the other is statistics of entrainment events identified in both regions.

a. Turbulent statistics

Fluxes of ozone, temperature, and momentum in the Cu and Sc regions are shown in Table 3. These fluxes are calculated from the cospectrum of vertical velocity and the corresponding variables and include contributions from fluctuations between 5-m and 3-km wavelengths. Table 3 shows that ozone flux in the Cu region is considerably larger than that in the Sc region. This is especially true on leg 4, where the ozone flux in the Cu region is nearly twice that in the Sc region. The larger ozone flux in the Cu region suggests stronger entrainment, as is seen from the entrainment velocity w_e (Table 3). This variable is calculated from the relation

$$w_e = -\frac{\overline{w'O_3'}}{\Delta O_3}, \qquad (1)$$

where ΔO_3 is the ozone increase across the inversion base. Here, ΔO_3 is obtained from the ozone profile in Fig. 2 (9 ppbv). The same ozone jump is used for both regions. The entrainment velocity in Table 3 is less than a centimeter per second, although it is about 20% larger in the Cu region than that found in the surrounding stratocumulus top. We also note that in the Cu region the ozone flux decreases only slightly from near cloud top (leg 5) to the level of leg 4, while in the Sc region ozone flux decreases much more rapidly. The ozone fluxes in the Sc region are consistent with a decoupled layer 300 to 400 m beneath leg 4, while those in the Cu region are consistent with a flux profile extending through the entire boundary layer since ozone fluxes at the ocean surface are small (Kawa and Pearson 1989).

A larger potential temperature flux is seen in the Sc region on the two in-cloud legs. This is consistent with radiative cooling being the major source of buoyancy flux for the Sc region. As entrainment is increased in the Cu region, one might expect a larger sensible heat flux due to evaporative cooling of the mixture of the inversion air and the boundary-layer air. However, this assumes that the entrained air becomes well mixed and saturated. This is an issue that needs to be further studied.

b. Statistics of entrainment events

Entrainment events are identified by using a conditional sampling method described by Khalsa (1993) and Wang and Albrecht (1994). Here, we use a procedure similar to that used in Wang and Albrecht (1994), except that only negative vertical velocity and positive ozone perturbations are used to identify the entrainment events. Moisture is not used here as an indicator of entrainment because of unreliable in-cloud measurements by the Lyman-alpha hygrometer. The mean characteristics of such defined entrainment events are given in Table 4, which shows that the geometric characteristics of entrainment events in the Cu and Sc regions are nearly the same. The entrainment events generally have a diameter of over 200 m and occupy a length fraction of around 30%. The vertical velocity of the entrainment events is also comparable in the two regions, although there is an increase in the magnitude

TABLE 3. Turbulence statistics in the Cu and Sc regions from legs 4 and 5. The ozone flux is in units of m s^{-1} ppbv, potential temperature flux in m s^{-1} K, momentum flux in m^2 s^{-2}, and w_e in m s^{-1}. Here, u and v denote the alongwind and crosswind components.

Leg	Region	$\overline{w'O_3'}$	$\overline{w'\theta'}$	$\overline{w'u'}$	$\overline{w'v'}$	w_e
Leg 4	Cu	−0.057	0.0025	−0.0284	−0.0263	—
	Sc	−0.028	0.0180	0.0077	−0.0032	—
Leg 5	Cu	−0.061	0.0101	0.0226	−0.0014	0.68
	Sc	−0.049	0.0170	0.0102	−0.0020	0.54

TABLE 4. Mean characteristics of entrainment events on legs 4 and 5. Here d is the mean width of the events. The brackets $\langle\ \rangle$ denotes the mean perturbations in the entrainment events.

Leg	Region	d (m)	Fraction	$\langle w' \rangle$ (m s^{-1})	$\langle O_3' \rangle$ (ppbv)	$\langle \theta' \rangle$ (K)
Leg 4	Cu	218	27.1	−0.40	0.30	−0.003
	Sc	221	28.5	−0.34	0.13	−0.032
Leg 5	Cu	214	27.3	−0.28	0.40	−0.025
	Sc	208	33.8	−0.29	0.27	−0.056

of w fluctuation from near cloud top (leg 5) to the lower level (leg 4), and the increase is more than twice as large in the Cu region compared with the Sc region. This increase in vertical velocity magnitude may be viewed as either acceleration of entrainment events away from the cloud top or deceleration of convective elements from below, which may originate near or below cloud base. The largest difference between the Cu and Sc regions lies in ozone fluctuations. On leg 5, the mean ozone perturbation in entrainment events is 0.40 ppbv, about 33% higher than that in the Sc region (0.27 ppbv), denoting the same percentage of increase in entrainment of inversion air. These values of ozone perturbation give a mixing fraction of 0.044 and 0.030 in Cu and Sc regions, respectively. Here the mixing fraction ϵ is defined as $\epsilon = \langle O_3' \rangle / \Delta O_3$, where the bracket ($\langle\ \rangle$) denotes the mean perturbation in entrainment events and ΔO_3 is the jump in ozone across the inversion base (9 ppbv). The ozone perturbation also decreases by nearly 33% on leg 4 in the Cu region from its cloud-top value, whereas in the Sc region it decreases by 50%. The variations of ozone with height and in the Cu and Sc regions are consistent with those of total ozone flux discussed earlier, which suggests that the entrainment events we have identified are largely responsible for ozone transport.

Unfortunately, virtual potential temperature perturbations in the entrainment events are not available here. It is therefore difficult to diagnose and compare the buoyancy of entrainment events in each region. The fluctuations of potential temperature (Table 4) show that the Sc region always has cooler entrainment events compared with the Cu region. In fact, the variance of θ in the entire Cu region is smaller than that in the Sc region. The reason for this is not clear. Nevertheless, as mentioned in the discussion of potential temperature flux, the smaller perturbations of θ in the Cu region do not necessarily indicate less buoyant entrainment events since moisture contributions to the buoyancy are not included.

It is interesting to compare the properties of entrainment events obtained during this ASTEX case with those obtained from FIRE. Wang and Albrecht (1994) analyzed entrainment events in a nocturnal stratocumulus-topped boundary layer observed during FIRE [First ISCCP (International Satellite Cloud Climatology Project) Regional Experiment]. The entrainment events found here generally are over 200 m in size and occupy about 30% of the total length of the leg, while those found during FIRE are less than 200 m and have length fraction of around 20%. The mean mixing fraction in entrainment events in FIRE was about 0.021, compared with 0.044 in the Cu region and 0.030 in the Sc region in ASTEX. These results are consistent with more entrainment in the ASTEX case.

c. Discussion

Entrainment is generally initiated by perturbations at the interface between the boundary-layer top and the inversion base. These perturbations may be caused by overshooting updrafts from the boundary layer, horizontal wind shear, breaking of gravity waves near the interface, or generation of buoyancy by radiative cooling at cloud top. Once the inversion air is entrained into the boundary layer, the mixture of the entrained air and the boundary-layer air may become negatively buoyant through buoyancy reversal under certain cloud-top jump conditions (e.g., Siems et al. 1990; Wang and Albrecht 1994), which may in turn enhance entrainment at the cloud top. Here, we look into several aspects of the turbulence field that may cause stronger entrainment at the cumulus cloud top. The possible change in the magnitude of buoyancy reversal at the cumulus top will be discussed in the last section.

We first examine the role of strong updrafts on the highest turbulence leg (leg 5) in the two regions that may overshoot the inversion base. We chose an arbitrary threshold for event mean vertical velocity of $0.5w_*$ to define the strong updrafts, where w_* is the convective velocity obtained from the buoyancy flux (the potential temperature flux is used for the in-cloud legs) profile in the entire boundary layer. Here, w_* was calculated to be 0.57 m s^{-1}. In the Cu region, about 44% of the updrafts exceed this threshold, while in the Sc region only 39% do. If the threshold is raised to 0.5 m s^{-1} ($0.89w_*$), 9% of the updrafts in the Cu region can be categorized as strong updrafts but none in the Sc region. Therefore, although the mean updraft vertical velocity in the two regions is found to be nearly the same (Table 2), there are stronger updrafts in the Cu region that may overshoot into the inversion and cause stronger entrainment at the cumulus top compared with that at the stratocumulus top.

The momentum fluxes in the Cu region are also considerably larger than those in the Sc region for both

legs 4 and 5 (Table 3). For leg 5, the alongwind stress component (the alongwind direction is estimated from the mean boundary-layer wind vector in each region) is more than twice that of the Sc region. Similarly, the momentum flux on the lower in-cloud leg is also larger in the Cu region. This again indicates that entrainment is larger for the Cu region. A large change in horizontal wind direction with height is observed in the sounding taken after the horizontal flight legs studied here. However, the wind speed is generally light on this flight, so the wind shear is not likely to be the major cause of strong entrainment at the cumulus top.

7. Horizontal variations of scalars

The horizontal variations of temperature, total water substance, and ozone in the two in-cloud legs are shown in Fig. 7. To emphasize the larger-scale variations in these scalars, fluctuations on scales smaller than 3 km are removed. The Cu and Sc regions are indicated on these graphs.

Large variations in all three scalars are observed at both levels in the cloud layer. The differences between the maximum and minimum values of potential temperature, total water substance, and ozone on leg 5 are 1.3 K, 1.5 g kg^{-1}, and 10 ppbv (Fig. 7b), respectively. Similar values are also found on leg 4, about 300 m below the cloud top (Fig. 7a). As far as we know, such substantial horizontal variations of scalar variables have never been documented before in stratocumulus-topped boundary layers over the ocean. Close inspection of the time series (Figs. 7a,b, and tabulated for convenience in Table 5) indicate that the highest temperature and moisture and the lowest ozone concentration are found in the Cu region on both legs.

TABLE 5. The mean potential temperature θ, ozone concentration O_3, and specific humidity q in the Cu and Sc regions on legs 4 and 5.

Leg	Region	$\overline{\theta}$ (K)	$\overline{O_3}$ (ppbv)	$\overline{q}$ (g kg^{-1})
Leg 4	Cu	291.2	40.2	7.6
	Sc	290.7	42.8	7.0
Leg 5	Cu	291.5	38.9	7.5
	Sc	290.8	40.2	7.1

Since strong entrainment would result in high ozone and low moisture in the boundary layer, the low-ozone and high-moisture characteristics in the Cu region appear at first to be contradictory to the results from the previous section that stronger entrainment may occur in the Cu region compared to the Sc region. However, even more important is the extent of the vertical mixing. In section 5, we show that the cloud layer is generally decoupled from the near-surface air except in the Cu region. Therefore, turbulent mixing in the Cu region includes surface air, while that in the Sc region does not. Consequently, the Cu region is a mixture of entrained inversion air and air from the entire boundary layer from the sea surface to the cloud top. While the entrained air is dry and high in ozone, the air near the sea surface is moist and low in ozone. Mixing with the near-surface air in the Cu region will, therefore, lower the ozone concentration and moisten the air. Here, mixing with the surface air dominates that from mixing with the inversion air in the Cu region, so that higher

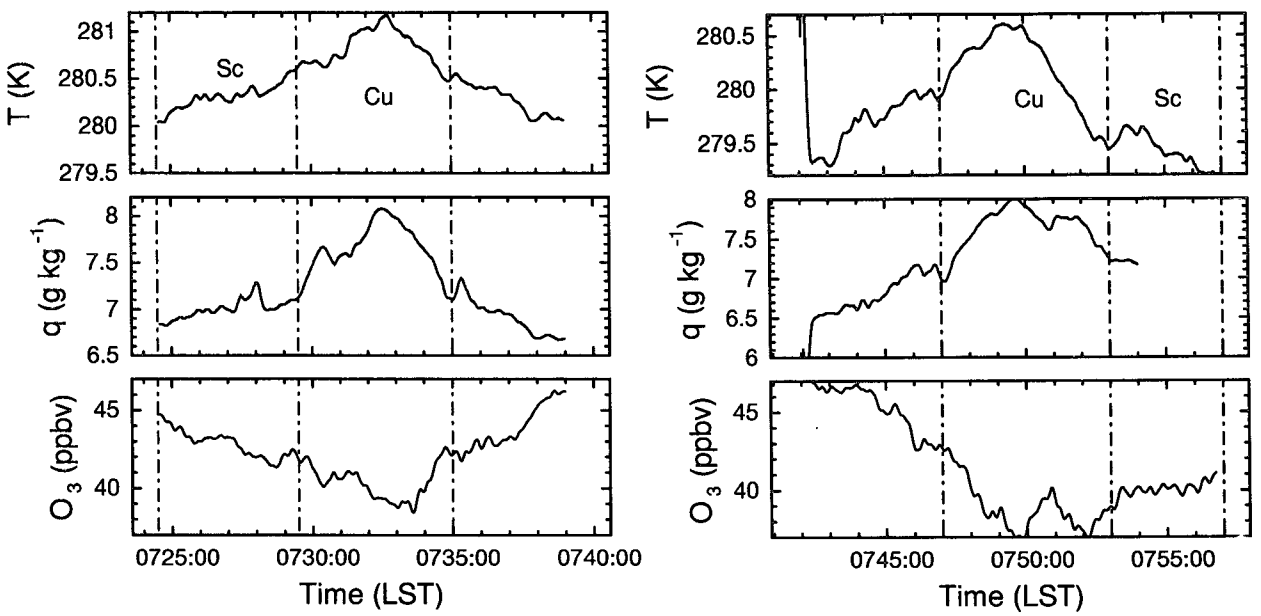

FIG. 7. (a) Horizontal variations of temperature, specific humidity, and ozone on leg 4. Contributions from perturbations at scales smaller than 3 km are removed. (b) Same as (a) except on leg 5.

moisture and lower ozone concentration result compared to the Sc region, which does not mix with air from below the decoupling transition.

This result can also be interpreted from the standpoint of the intermittency of the exchange process by penetrating cumulus clouds. In the upper boundary layer above the decoupling transition, the entrainment fluxes in the Cu and Sc regions are of the same order of magnitude, although entrainment at the Cu top may be larger than at the Sc top. The fluxes coming from below the decoupling transition, however, are distinctly different in the two regions. Since the boundary layer in the Sc region is decoupled, flux transport across the decoupling transition is very small. Significant flux transport occurs only in the Cu region, where low ozone and moist air from the near-surface layer are transported into the upper boundary layer. The difference in flux transport from below in the two regions can be much larger than for the entrainment flux. As a result, in the cumulus region mixing with the surface air dominates mixing with the entrained inversion air in the upper boundary layer.

8. Summary and discussions

In this paper, aircraft measurements in a cumulus cloud penetrating through the surrounding stratocumulus are analyzed. We emphasize the differences in turbulent mixing and cloud-top entrainment due to cumulus cloud through comparisons between a cumulus region and a noncumulus (stratocumulus) region. The stratocumulus boundary layers observed during ASTEX were often decoupled from the surface air, except in regions of cumulus penetration. As a result, complete mixing in the entire boundary layer occurs in the Cu region, where water vapor mixing ratio and ozone concentration are affected by both entrainment at the cloud top and surface processes. In the decoupled stratocumulus region, the entrained dry and high-ozone air is confined to the cloud mixed layer, while moisture input from the surface is confined to the subcloud layer. This difference in the two regions results in large horizontal variability in ozone and total water substance. Using turbulence statistics and conditional sampling of entrainment events in the two regions, we find evidence that entrainment at the cumulus top may be stronger than that at the stratocumulus top. However, the analysis of cloud-top entrainment is complicated by insufficient sampling of cloud-top jump conditions in the two regions. One way that this could be addressed in the future is to consider using a trace chemical species that is released at the sea surface and has an atmospheric lifetime of 10^4–5×10^5 s; that is, long enough for it to be distributed throughout the boundary layer, but short enough that it would have negligible concentration above the boundary layer. Dimethyl sulfide is a candidate species. In addition, it is negligibly soluble in cloud water. Such a tracer should also be useful in distinguishing between penetrating cumuli and stratocumulus regions because of their differences in mixing time with surface air.

The large horizontal variations in moisture and temperature, which are caused mainly by the differences in the vertical extent of turbulent mixing in the boundary layer, may have a feedback on entrainment at the cloud top. Table 5 shows that the Cu region has a higher temperature and is more moist than the Sc region. This variation suggests that it may not always be true to assume the same cloud-top jump conditions in the Cu and Sc regions. If we assume that the conditions above the boundary layer are the same in both regions (we do not have measurements to confirm this), the Cu region then has a smaller increase in temperature and larger decrease in specific humidity compared to the Sc region, which indicates stronger buoyancy reversal (or more negative buoyancy through entrainment mixing) in the Cu region (Siems et al. 1992; Wang and Albrecht 1994). Buoyancy reversal may in turn affect cloud-top entrainment and turbulent mixing in the boundary layer (Wang and Albrecht 1994). Therefore, the existence of penetrating cumuli may change the nature of cloud-top entrainment instability in the penetrating Cu region. However, there are generally substantial horizontal variations in chemical and meteorological conditions in the air above the inversion, which makes this issue difficult to quantify (e.g., Paluch et al. 1992). We do note that these horizontal changes in buoyancy can accentuate any mesoscale circulation associated with the penetrating Cu in the manner discussed by Paluch and Lenschow (1991). Horizontal variability can also affect our estimates of the difference in w_e and mixing fraction between the two regions and is an area that requires further research. Nevertheless, the preponderance of evidence points to the Cu region having a larger entrainment velocity than the Sc region.

We see from this study that the Cu region is the conduit that connects the near-surface air to the cloud layer, so that moisture can be transported from the surface to the upper layer. The low-level convergent flow brings in moisture from the surroundings, while the upper divergent flow spreads moisture from the Cu region to the surrounding stratocumulus layer. Therefore, the penetrating cumuli supply moisture to the upper stratocumulus cloud, which might otherwise dissipate in a decoupled environment.

We provide evidence of how penetrating cumuli modify the stratocumulus-topped boundary layer and help to explain the existence of penetrating cumuli and the overlying stratocumulus decks. The penetrating cumuli discussed here are different from those observed previously near the California coast (Q. Wang 1993) or over the North Sea (Nicholls 1984). The cumulus clouds here show strong mesoscale organizations and have substantial dynamic effects on the boundary layer and cloud structure. Important questions such as how the cumuli form and how the overlying stratocumulus

clouds eventually dissipate still remain. Further observational studies would be useful to fully understand the stratocumulus to trade cumulus transition. Analyses of measurements along a low-level trade wind trajectory (a Lagrangian experiment) may be useful for this purpose.

Acknowledgments. We thank Chin-Hoh Moeng, Margaret LeMone, Chris Bretherton, Shouping Wang, Mark Miller, and Ilga Paluch for interesting and insightful discussions. The efforts of Richard Schillawski, who collected and calibrated the ozone data, are greatly appreciated. We also thank Bruce Albrecht and the other reviewer for their thorough reviews and valuable suggestions. Qing Wang is supported by a fellowship from the Advanced Study Program at NCAR. Part of this work was supported by ONR N00014-90-F0037 under Interagency Agreement 89-12.

REFERENCES

Albrecht, B. A., A. K. Betts, W. Schubert, and S. K. Cox, 1979: A model of the thermodynamic structure of the trade-wind boundary layer: Part II. Applications. *J. Atmos. Sci.,* **36,** 90–98.

Betts, A. K., 1990: Diurnal variation of California coastal stratocumulus from two days of boundary layer soundings. *Tellus,* **42A,** 302–304.

Bluth, R. T., and B. A. Albrecht, 1993a: Atlantic Stratocumulus Transition Experiment and Marine Aerosol and Gas Exchange. June 1992 experiment summary, Part I—Mission summaries. Dept. of Meteorology Rep., The Pennsylvania State University, University Park, PA, 286 pp.

——, and ——, 1993b: Atlantic Stratocumulus Transition Experiment and Marine Aerosol and Gas Exchange. June 1992 experiment summary, Part II—Platform operations. Dept. of Meteorology Rep., The Pennsylvania State University, University Park, PA, 277 pp.

Bretherton, C. S., 1992: A conceptual model of the stratocumulus-trade-cumulus transition in the subtropical oceans. *Proc., 11th Int. Conf. on Clouds and Precipitation,* Vol. 1, Montreal, Quebec, Canada, International Commission on Clouds and Precipitation and International Association of Meteorology and Atmospheric Physics, 374–377.

——, 1993: Understanding Albrecht's model of trade wind cumulus cloud fields. *J. Atmos. Sci.,* **50,** 2264–2283.

Hanson, H. P., 1991: Marine stratocumulus climatologies. *Int. J. Climatol.,* **11,** 147–164.

Hignett, P., 1991: Observations of diurnal variation in a cloud-capped marine boundary layer. *J. Atmos. Sci.,* **48,** 1474–1482.

Kawa, S. R., and R. Pearson Jr., 1989: Ozone budgets from the dynamics and chemistry of marine stratocumulus experiment. *J. Geophys. Res.,* **92,** 9809–9817.

Khalsa, S. J. S., 1993: Direct sampling of entrainment events in a marine stratocumulus layer. *J. Atmos. Sci.,* **50,** 1734–1750.

Kropfli, R. A., and B. W. Orr, 1993: Observations of microcells in the marine boundary layer with 8-mm wavelength Doppler radar. Preprints, *26th Int. Conf. on Radar Meteorology,* Norman, OK, Amer. Meteor. Soc., 492–494.

Krueger, S. K., G. T. McLean, and Q. Fu, 1994: Boundary-layer circulation changes during the stratus-to-cumulus transition in the subtropical marine boundary layer. *J. Atmos. Sci.,* submitted.

LeMone, M. A., and W. T. Pennell, 1976: The relationship of trade cumulus distribution to subcloud layer fluxes and structure. *Mon. Wea. Rev.,* **104,** 524–539.

Lenschow, D. H., and P. Spyers-Duran, 1989: Measurement techniques: Air motion sensing. NCAR Research Aviation Facility Bulletin No. 23, 36 pp. [Available from NCAR, P.O. Box 3000, Boulder, CO 80307.]

Nicholls, S., 1984: The dynamics of stratocumulus: Aircraft observations and comparisons with a mixed layer model. *Quart. J. Roy. Meteor. Soc.,* **110,** 783–820.

Paluch, I. R., and D. H. Lenschow, 1991: Stratiform cloud formation in the marine boundary layer. *J. Atmos. Sci.,* **48,** 2141–2158.

——, ——, J. G. Hudson, and R. Pearson Jr., 1992: Transport and mixing processes in the lower troposphere over the ocean. *J. Geophys. Res.,* **97,** 7527–7541.

——, ——, S. Siems, S. McKeen, G. L. Kok, and R. D. Schillawski, 1994: Evolution of the subtropical marine boundary layer: Comparison of soundings over eastern Pacific from FIRE and HaRP. *J. Atmos. Sci.,* **51,** 1465–1479.

Pennell, W. T., and M. A. LeMone, 1974: An experimental study of turbulence structure in the fair weather trade wind boundary layer. *J. Atmos. Sci.,* **31,** 1308–1323.

Randall, D. A., 1980: Conditional instability of the first kind upside-down. *J. Atmos. Sci.,* **37,** 125–130.

Siems, S. T., C. S. Bretherton, M. B. Baker, S. Shy, and R. T. Breidenthal, 1990: Buoyancy reversal and cloud-top entrainment instability. *Quart. J. Roy. Meteor. Soc.,* **116,** 705–739.

Wang, Q., 1993: Turbulent mixing and transport in marine stratocumulus-topped boundary layers—An observational study. Ph.D. dissertation, The Pennsylvania State University, 199 pp.

——, and B. A. Albrecht, 1994: Observations of cloud-top entrainment in marine stratocumulus clouds. *J. Atmos. Sci.,* **51,** 1530–1547.

Wang, S., 1993: Modeling marine boundary-layer clouds with a two-layer model: A one-dimensional simulation. *J. Atmos. Sci.,* **50,** 4001–4021.

Warren, S., C. J. Hahn, J. London, R. M. Chervin, and R. L. Jenne, 1989: Global distribution of total cloud cover and cloud type amounts over the ocean. NCAR Tech. Note TN-317+STR, 150 pp.